JACS
JOURNAL OF THE AMERICAN CHEMICAL SOCIETY
Article
pubs.acs.org/JACS

Extraordinary Off-Stoichiometric Bismuth Telluride for Enhanced n-Type Thermoelectric Power Factor

Kunsu Park,[†,‡,#] Kyunghan Ahn,[‡,#] Joonil Cha,[†,‡] Sanghwa Lee,[†,‡] Sue In Chae,[†,‡] Sung-Pyo Cho,[§] Siheon Ryee,[∥] Jino Im,[⊥] Jaeki Lee,[∇] Su-Dong Park,[∇] Myung Joon Han,[∥] In Chung,[*,†,‡] and Taeghwan Hyeon[*,†,‡]

[†]Center for Nanoparticle Research, Institute for Basic Science (IBS), Seoul 08826, Republic of Korea

[‡]School of Chemical and Biological Engineering and Institute of Chemical Processes, and [§]National Center for Inter-University Research Facilities, Seoul National University, Seoul 08826, Republic of Korea

[∥]Department of Physics and KAIST Institute for the NanoCentury, Korea Advanced Institute of Science and Technology, Daejeon 34141, Republic of Korea

[⊥]Thin Film Materials Research Center, Korea Research Institute of Chemical Technology, Daejeon 34114, Republic of Korea

[∇]Creative Research Center, Creative and Fundamental Research Division, Korea Electrotechnology Research Institute (KERI), Changwon 51543, Gyeongsangnam-do, Republic of Korea

Supporting Information

ABSTRACT: Thermoelectrics directly converts waste heat into electricity and is considered a promising means of sustainable energy generation. While most of the recent advances in the enhancement of the thermoelectric figure of merit (ZT) resulted from a decrease in lattice thermal conductivity by nanostructuring, there have been very few attempts to enhance electrical transport properties, i.e., the power factor. Here we use nanochemistry to stabilize bulk bismuth telluride (Bi_2Te_3) that violates phase equilibrium, namely, phase-pure n-type $K_{0.06}Bi_2Te_{3.18}$. Incorporated potassium and tellurium in Bi_2Te_3 far exceed their solubility limit, inducing simultaneous increase in the electrical conductivity and the Seebeck coefficient along with decrease in the thermal conductivity. Consequently, a high power factor of ~43 μW cm^{-1} K^{-2} and a high ZT > 1.1 at 323 K are achieved. Our current synthetic method can be used to produce a new family of materials with novel physical and chemical characteristics for various applications.

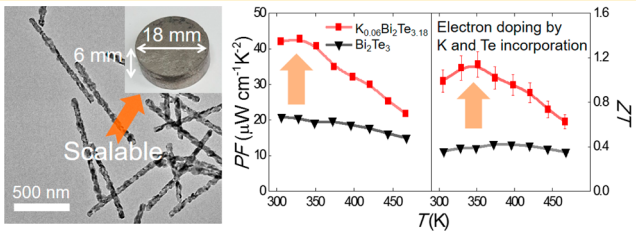

INTRODUCTION

Thermoelectric (TE) technology enables direct conversion between heat and electricity and is consequently considered a promising means of sustainable power generation and energy saving. The efficiency of TE conversion is defined by the dimensionless figure of merit $ZT = \sigma S^2T/\kappa$, where σ is the electrical conductivity, S is the Seebeck coefficient, κ is the thermal conductivity, T is the absolute temperature, and the product σS^2 is the power factor (PF).[1−3] Previous advances for enhancing ZT are mostly attributed to reduction in lattice thermal conductivity (κ_{latt}) by various strategies, including nanostructuring,[4−19] hierarchical architecturing,[20−22] using intrinsically low κ_{latt} materials,[23−29] inclusion of guest species in the cages of materials,[30−38] ball-milling,[39,40] and melt-spinning.[41] Unfortunately, κ_{latt} of state-of-the-art TE materials approaches a lower fundamental limit. In contrast, PF does not have a theoretical upper limit, thereby allowing much greater room for improvement of ZT. However, σ and S are inversely proportional to each other, making it very difficult to increase PF. Indeed, there are few strategies for the enhancement of PF,[42−49] which is regarded as one of the most important issues for all TE materials because high PF is an ultimate solution for achieving high ZT and essential for realizing high performance during power generation.

Bi_2Te_3-based compounds are representative TE materials operating near room temperature.[50] There are two major challenges that have to be solved for these room temperature TE materials. First, very few dopants and substituents have proven effective in enhancing ZT.[51,52] Second, the poorer performance of n-type Bi_2Te_3-based materials than that of p-type materials seriously limits their practical applications because TE modules consist of junctions of n- and p-type TE materials, and the worse counterpart determines the overall module efficiency.

Here we report that we go beyond compositional limitations stringently regulated by phase equilibrium and stabilize extraordinary off-stoichiometric compounds through a nano-chemical synthetic method. Remarkably, the bulk $K_{0.06}Bi_2Te_{3.18}$ (bulk KBT), despite considerable deviation from the elemental

Received: September 2, 2016
Published: October 20, 2016

 © 2016 American Chemical Society
DOI: 10.1021/jacs.6b09222
J. Am. Chem. Soc. 2016, 138, 14458−14468

Scheme 1. Schematic Illustration of Syntheses for $Bi_2Te_{3.14}$ Nanotubes (BT Nanotube), K-Incorporated $K_{0.07}Bi_2Te_{3.14}$ Nanotubes (KBT Nanotube), Consolidated Bulk $Bi_2Te_{3.14}$ (Bulk BT), and Consolidated Bulk $K_{0.06}Bi_2Te_{3.18}$ (Bulk KBT)

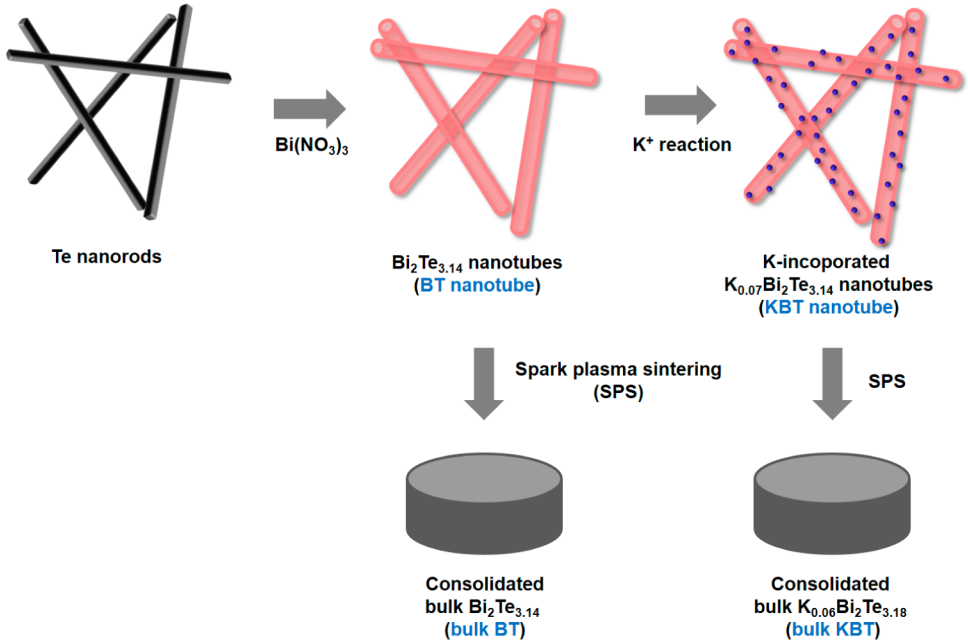

ratio permitted by the phase diagram, shows high phase homogeneity and thermal stability. In contrast, the sample with a similar nominal composition prepared using a conventional high-temperature solid-state reaction contains excess tellurium that decomposes upon heating. Due to the presence of electron donating potassium dopants, the polycrystalline bulk KBT sample with a highly preferential orientation exhibits a surprisingly high *PF* of ~43 μW cm^{-1} K^{-2}, rivaling that of a single crystal $Bi_2Te_{3-x}Se_x$, and consequently one of the highest *ZT* (>1.1) among n-type TE materials that operate near room temperature. Very importantly, we use spherical aberration-corrected high-angle annular dark-field scanning transmission electron microscopy (Cs-corrected HAADF-STEM) combined with energy dispersive X-ray spectroscopy (EDS) and electron energy loss spectroscopy (EELS) to characterize the locations of excess potassium and tellurium atoms, which allows us to clearly explain the unusual compositions and the resulting excellent TE performance. Our new approach enables the synthesis of solid-state materials whose compositions cannot be stabilized according to phase equilibrium and consequently the realization of enhanced properties. Furthermore, this method can be generalized to a wide range of materials for various applications, not just limited to bismuth telluride for TE applications.

■ RESULTS AND DISCUSSION

The seemingly obvious way of obtaining n-type Bi_2Te_3 is the addition of excess tellurium as an electron donor to produce Bi_2Te_{3+y}. However, the phase diagram of the Bi−Te binary system allows a limited range of the Bi:Te stoichiometry from 2:2.98 to 2:3.02 (Figure S1).[53] Therefore, it is very difficult to incorporate a large excess of tellurium to provide enough electron carriers to achieve a high *ZT* by conventional synthetic methods. We overcome this problem by utilizing a nano-chemical approach that is kinetically controllable at the atomic level.

$Bi_2Te_{3.14}$ nanotubes were synthesized from Te nanorods using a two-step procedure that was modified from a previously reported method (Scheme 1).[54] We synthesized polyvinylpyrrolidone (PVP)-stabilized Te nanorods with a typical length of ~1 μm and a diameter of 50 nm. The as-synthesized Te nanorods were reacted with $Bi(NO_3)_3$ to produce Bi_2Te_3 nanotubes. To achieve a tellurium-rich phase, we performed the synthesis at a relatively low temperature of 160 °C to stabilize excess tellurium in the Bi_2Te_3 structure. In addition, PVP ligands act as a diffusion barrier, which slows down the reaction between Bi^{3+} and Te^{2-} ions and causes the Kirkendall effect.[55] The outward diffusion of Te^{2-} ions proceeds relatively faster than the inward diffusion of Bi^{3+} ions, forming hollow Bi_2Te_3 nanotubes with kinetically stabilized excess tellurium. The chemical composition is determined to be $Bi_2Te_{3.14}$ by inductively coupled plasma atomic emission spectroscopy (ICP-AES), demonstrating the incorporation of excess tellurium (Table S1). The bismuth telluride nanotubes have a polycrystalline nature, being composed of nanoplates with a thickness of ~10−20 nm, and they accordingly have a rough and defective morphology. Their typical length and diameter are ~1 μm and ~70 to 80 nm, respectively, as shown in transmission electron microscopy (TEM) (Figure 1) and scanning electron microscopy (SEM) images (Figure S2). Their hollow structures can be clearly seen in scanning transmission electron microscopy (STEM) images and EDS (Figure S3). PVP derivatives still remain after washing, as observed in the Fourier transform infrared spectroscopy (FT-IR) spectrum (Figure S4). Because such organic residues can give rise to high electrical resistivity, we replace them with a substituent that can contribute to improving n-type TE performance. $Bi_2Te_{3.14}$ nanotubes were reacted with KOH to facilitate an ion-exchange reaction between residual PVP and potassium cations. This KOH treatment is a critical step for synthesizing the final bulk KBT, because not only does it remove residual PVP, but it also enables the incorporation of potassium cations. Thermogravimetric analysis (TGA) shows

DOI: 10.1021/jacs.6b09222
J. Am. Chem. Soc. 2016, 138, 14458−14468

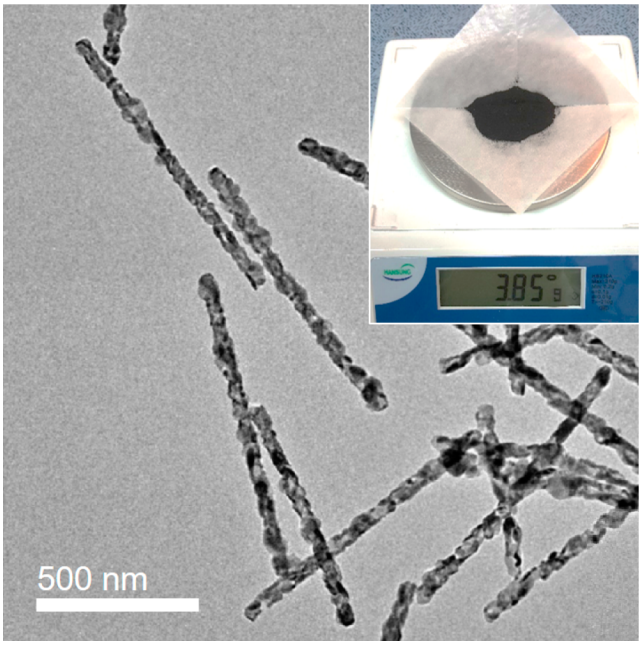

Figure 1. Representative transmission electron microscopy (TEM) image of the KBT nanotubes. A typical production scale for the nanotubes is ~4 g per batch (inset).

~40% of PVP residues are removed by the reaction (Figure S5). ICP-AES analysis gives the composition of "$K_{0.07}Bi_2Te_{3.14}$". Powder X-ray diffraction (XRD) patterns of "$Bi_2Te_{3.14}$" and "$K_{0.07}Bi_2Te_{3.14}$" nanotubes correlate well with those of theoretical calculations, with no evidence of Te and K_2Te impurities (Figure S6).

The synthesis of tellurium-rich and potassium-incorporated bismuth telluride nanotubes is highly reproducible and scalable with production of ~4 g per batch (Figure 1, inset). The nanopowder was pressed into a dense bulk pellet (>95% theoretical density) by spark plasma sintering (SPS), consequently converting the nanopowder into bulk form. The resulting bulk pellet was cut and polished perpendicular and parallel to the pressing direction of SPS for further characterization (Figure 2). We also prepared control samples of stoichiometric Bi_2Te_3 as well as tellurium-excess $Bi_2Te_{3.05}$ and $Bi_2Te_{3.14}$ (nominal composition) using high-temperature solid-state reactions. ICP-AES analysis reveals that the bulk samples generated from the SPS of the $Bi_2Te_{3.14}$ nanotubes (BT nanotube) and $K_{0.07}Bi_2Te_{3.14}$ nanotubes (KBT nanotube) have

Figure 2. Typical dense pellet of bulk KBT by SPS with a typical diameter of 18 mm and a thickness of ~6 mm to 7 mm (left) and specimens cut for measuring electrical (bars, middle) and thermal transport properties (disk, right).

chemical compositions of $Bi_2Te_{3.14}$ (bulk BT) and $K_{0.06}Bi_2Te_{3.18}$ (bulk KBT), respectively. Surprisingly, both nanotubes and their bulk counterparts do not show any evidence of isolated tellurium according to XRD studies (Figure 3a). In contrast, the control "$Bi_2Te_{3.05}$" sample shows the peak at 23°, which corresponds to the (001) reflection of tellurium. Furthermore, TGA data reveals that the control $Bi_2Te_{3.05}$ sample shows a weight loss above ~680 K upon heating under Ar flow, as elemental tellurium does, suggesting the decomposition of excess tellurium, which has a melting point of 720 K. In contrast, the bulk KBT sample does not show noticeable weight loss up to 800 K (Figure 3b). According to differential scanning calorimetry data, the bulk BT and KBT as well as the control stoichiometric Bi_2Te_3 show single melting behaviors (Figure 3c). In contrast, the control tellurium-rich $Bi_2Te_{3.05}$ and $Bi_2Te_{3.14}$ melt incongruently, exhibiting the additional endothermic peak for the melting of tellurium at 688 K, which is in agreement with the TGA results. The thermal analysis of bulk BT and KBT reveals their high thermal stability and phase-homogeneity despite the inclusion of excess potassium and tellurium. These data clearly demonstrate that our nanochemical method enables the synthesis of off-stoichiometric compounds that violate the phase diagram of the constituent elements. TGA and FT-IR data (Figures S5 and S7) reveal that the samples after SPS contain a negligible amount of organic residues that are considered a serious problem for solution-processed materials for TE applications. The XRD pattern of the bulk KBT taken perpendicular plane to the pressing direction of SPS shows a highly preferred orientation of (00*l*) reflections in comparison to that measured parallel plane to the pressing direction of SPS (Figure 4). This result clearly demonstrates that the one-dimensional nanotubes are well aligned to form a two-dimensional arrangement perpendicular to the pressing direction of SPS. SEM images also show a single crystal-like and highly oriented morphology of the bulk KBT sample (Figure 5). Theoretical calculations on the formation energy within the density functional theory (DFT) reveal that the composition corresponding to the highest solubility limit at 800 K is "$K_{0.0004}Bi_{1.9996}Te_{3.0073}$", suggesting that potassium and tellurium-rich Bi_2Te_3 cannot be obtained using conventional high-temperature solid-state reactions (Figures 9, S8, and S9).

We performed atomic resolution HAADF-STEM, EDS, and EELS studies on bulk BT and KBT samples to characterize how excess potassium and tellurium are stabilized and where they are located. All specimens for TEM studies are pellets that are pressed by SPS. Bi_2Te_3 features three hexagonally packed Te atomic layers that are interleaved by octahedral Bi atoms. Each Bi_2Te_3 layer is stacked by van der Waals interaction along the *c*-axis (Figure 6a). Conceptually, it is a defective NaCl-type (rock salt) structure. If we consider a "Na_3Cl_3" structure viewed along the [110] direction, removal of 1/3 of the Na atomic layer results in the Bi_2Te_3 structure. Consequently, the guest species can be inserted into the octahedral sites located between the layers (Figure 6b).

The cross-sectional HAADF-STEM image of the bulk BT viewed down the [−100] axis shows moderate structural dislocations propagating along the in-plane direction (Figures 7a and b). The enlarged image on the selected area clearly shows the typical lamellar structure of Bi_2Te_3 (Figure S10). Elemental mapping by STEM-EDS verifies the locations of Bi and Te atoms. In contrast, bulk KBT contains considerable lattice modulations along the in-plane direction, including merged lattices and antisites of Te and Bi (Figures 7c and d).

DOI: 10.1021/jacs.6b09222
J. Am. Chem. Soc. 2016, 138, 14458−14468

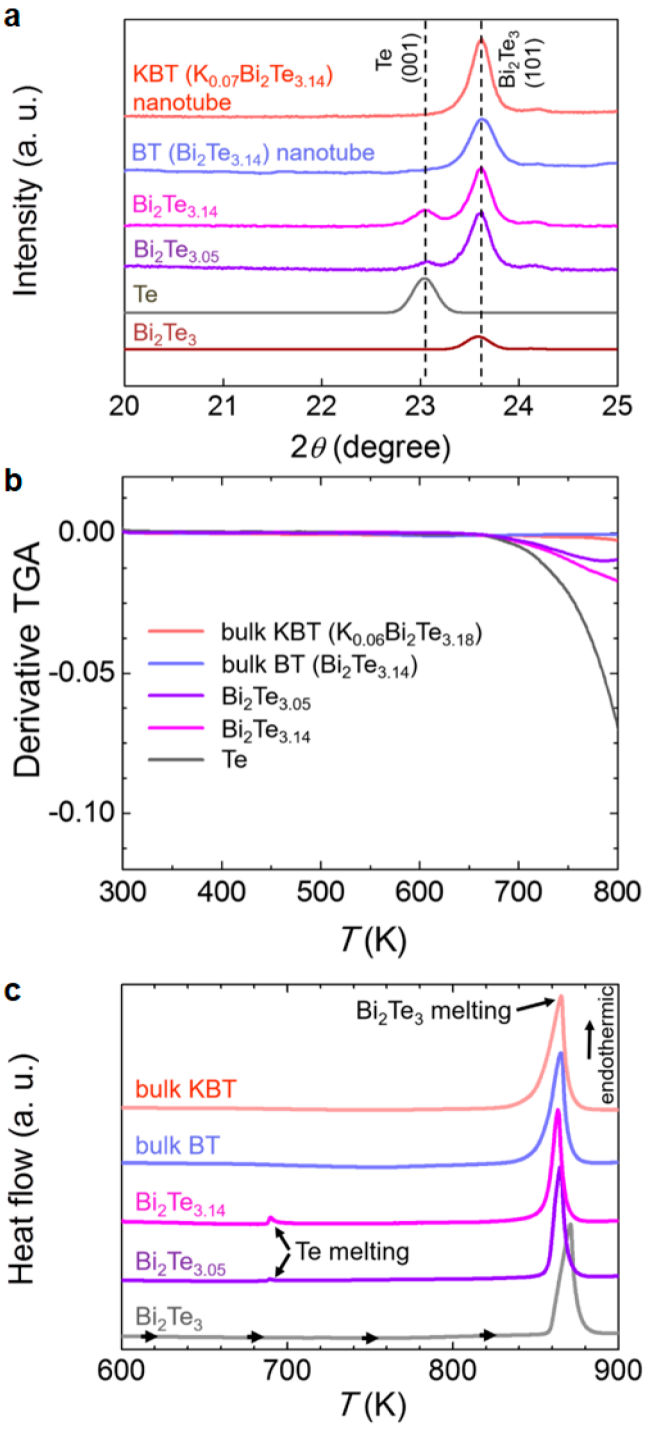

Figure 3. (a) Powder X-ray diffraction (XRD) patterns of BT and KBT nanotubes in comparison with those of control $Bi_2Te_{3.05}$ and $Bi_2Te_{3.14}$ samples containing excess tellurium. Theoretical patterns of Bi_2Te_3 (JCPDS 15-0863) and Te (JCPDS 36-1452) are given. The tellurium-rich control samples show the (001) reflection of hexagonal tellurium. (b) First derivative of the thermogravimetric analysis (TGA) curve, showing the thermal stability of bulk BT and KBT. The control $Bi_2Te_{3.05}$ and $Bi_2Te_{3.14}$ samples decompose by losing excess tellurium, as confirmed by the thermal behavior of tellurium (melitng point of Te ~ 720 K). (c) Differential scanning calorimetry analysis of Bi_2Te_3, bulk BT, and bulk KBT at a rate of 10 K min^{-1} in comparison with the control $Bi_2Te_{3.05}$ and $Bi_2Te_{3.14}$, demonstrating the phase-homogeneity of bulk BT and KBT.

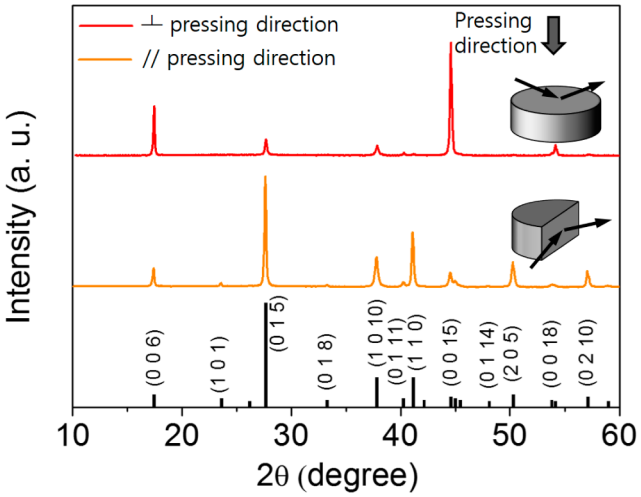

Figure 4. XRD patterns of bulk KBT taken perpendicular plane (upper, red) and parallel plane (middle, orange) to the pressing direction of SPS, respectively, showing the highly preferential orientation of the former. Standard reference XRD peaks are represented in black lines (JCPDS 15-0863).

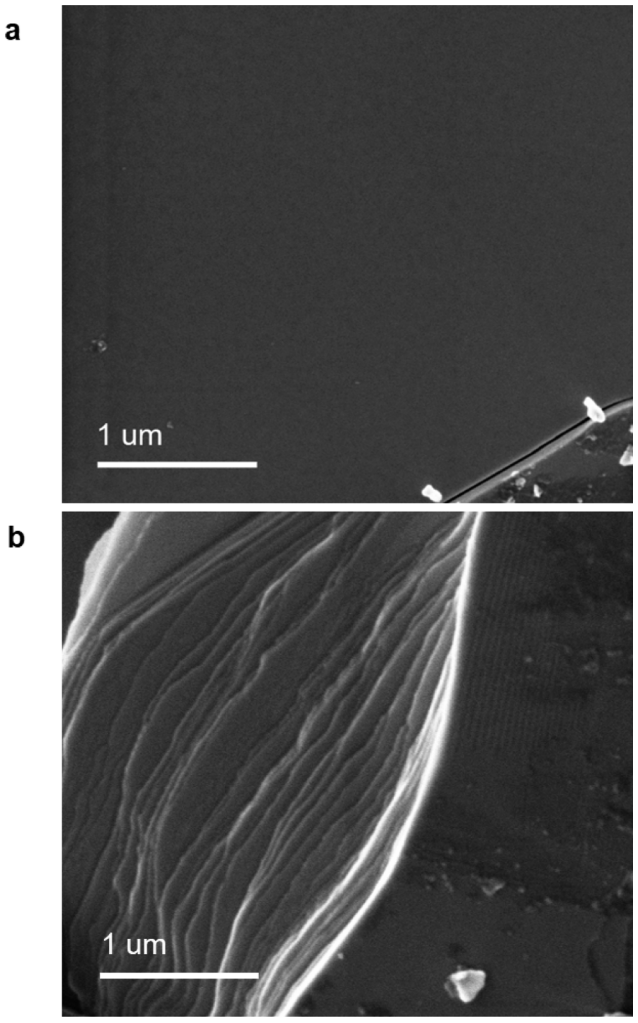

Figure 5. Representative SEM images of bulk KBT showing the highly oriented two-dimensional morphology of the SPS sample taken (a) perpendicular plane and (b) parallel plane to the pressing direction of SPS.

DOI: 10.1021/jacs.6b09222
J. Am. Chem. Soc. 2016, 138, 14458−14468

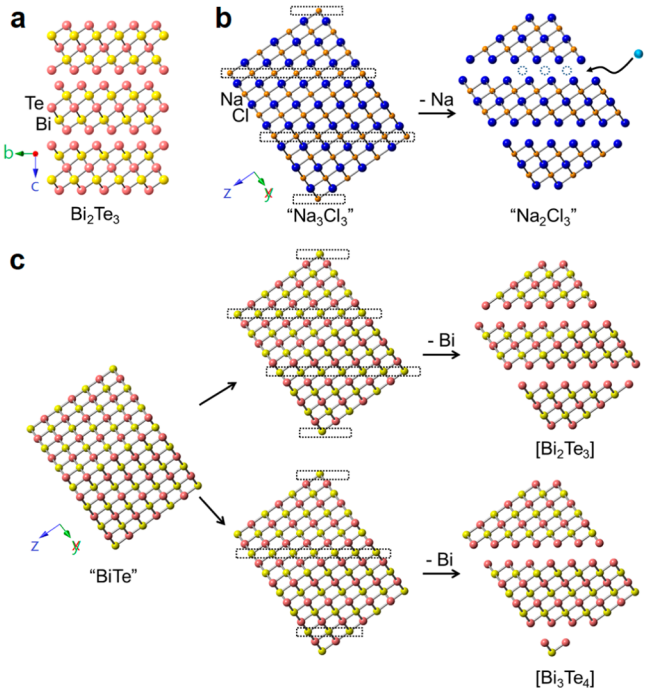

Figure 6. (a) Crystal structure of Bi_2Te_3. (b) Structural relationship between NaCl-type (rock salt) and Bi_2Te_3 showing Bi_2Te_3 is a defective NaCl-type structure and capable of accepting guest species in interlayer space. (c) Schematic diagram showing the formation of $[Bi_2Te_3]$ and $[Bi_3Te_4]$ structural motifs from "$Bi_\infty Te_\infty$" by deleting Bi atomic layers periodically.

The HAADF-STEM image in Figure 7e reveals that excess tellurium is intercalated in the interlayer space, thereby merging individual Bi_2Te_3 layers. Along with ideal quintuple atomic layers, extended septuple layers composed of (Te−Bi−Te−Bi−Te−Bi−Te) atomic arrangements are also frequently observed, and respective Bi and Te atoms are confirmed by elemental mapping using STEM-EDS (Figures 7d and S11). The observation of the $[Bi_3Te_4]$ layers can be understood in light of the defective NaCl structure of Bi_2Te_3 (Figure 6c). Elimination of every third Bi atomic layer from $[Bi_\infty Te_\infty]$ yields $[Bi_3Te_4]$ lattices, whereas elimination of every second Bi atomic layer leads to $[Bi_2Te_3]$ lattices. First-principles DFT calculations support that the formation of $[Bi_3Te_4]$ has a very low formation energy of 0.015 and 0.168 eV under bismuth-rich and tellurium-rich conditions, respectively.[56] Moreover, Figure 7d demonstrates that a single atomic layer of Te replaces that of Bi to occupy the Bi antisites, forming (Te−Bi−Te−Bi−Te−Te−Bi−Te) atomic arrangements, and EDS analysis in HAADF-STEM maps the locations of Bi and Te atoms. It should be noted that the formation of Q−Q bonds is common for chalcogen atoms (Q = S, Se, and Te). Polychalcogenide anions have the −2 formal charge, namely, $[Q_n]^{2-}$.[57] Accordingly, the formation of (Te−Te) atomic layers should reduce the net negative charge of bulk BT and KBT samples, which explains the stabilization of excess tellurium. Unusual structural domains found in the bulk KBT sample are unique to our synthetic method that provides kinetic control over a reaction between premade Te nanorods and a Bi precursor. As a result of the intercalated tellurium atoms, the interlayer gap increases from 0.27 to 0.35 nm.

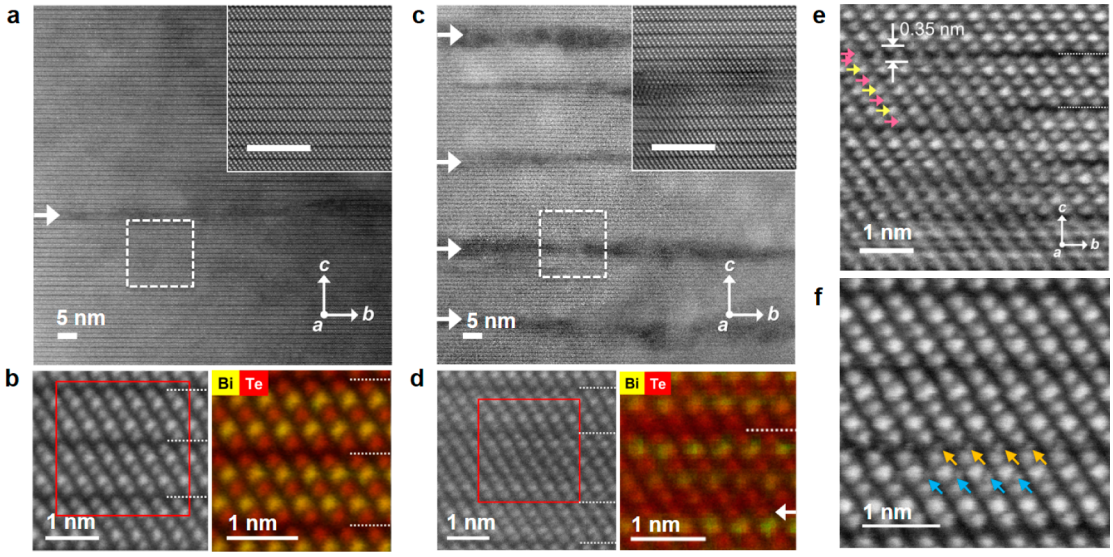

Figure 7. Cross-sectional scanning TEM (STEM) images and elemental mapping of bulk BT and KBT. (a) Typical low-magnification STEM image of bulk BT showing moderate structural dislocations propagating along the in-plane direction (white arrow). Inset: high-angle annular dark-field STEM (HAADF-STEM) image enlarged from the box showing the ideal Bi_2Te_3 structure, that consists of quintuple atomic layers of Bi and Te atoms stacked by van der Waals interactions along the *c* axis. (b) Elemental mapping of the bulk BT sample by STEM energy dispersive X-ray spectroscopy (STEM-EDS), clearly identifying Bi (yellow) and Te (red) atoms. van der Waals gaps are shown as dashed lines. (c) Typical low-magnification STEM image of bulk KBT. Structural modulations propagating along the in-plane direction are evident (white arrow). Inset: Enlarged image of the boxed region, clearly showing severe structural dislocations. (d) Elemental mapping of the bulk KBT sample examined by STEM-EDS, showing the (Te−Bi−Te−Bi−Te−Te−Bi−Te) atomic arrangement. An atomic layer of Te replacing that of Bi to form Te−Te bonds is clearly seen (white arrow). (e) HAADF-STEM image of bulk KBT, revealing a septuple atomic layer of $[Bi_3Te_4]$ in a structural motif and Te atoms intercalated in the van der Waals gap of Bi_2Te_3. The expanded interlayer distance of 0.35 nm due to Te intercalation is shown. Te and Bi atoms are indicated by pink and yellow arrows, respectively. (f) HAADF-STEM image of bulk KBT, showing potassium ions occupying the interstitial (blue arrow) and interlayer (orange arrow) sites of Bi_2Te_3 layers.

DOI: 10.1021/jacs.6b09222
J. Am. Chem. Soc. 2016, 138, 14458−14468

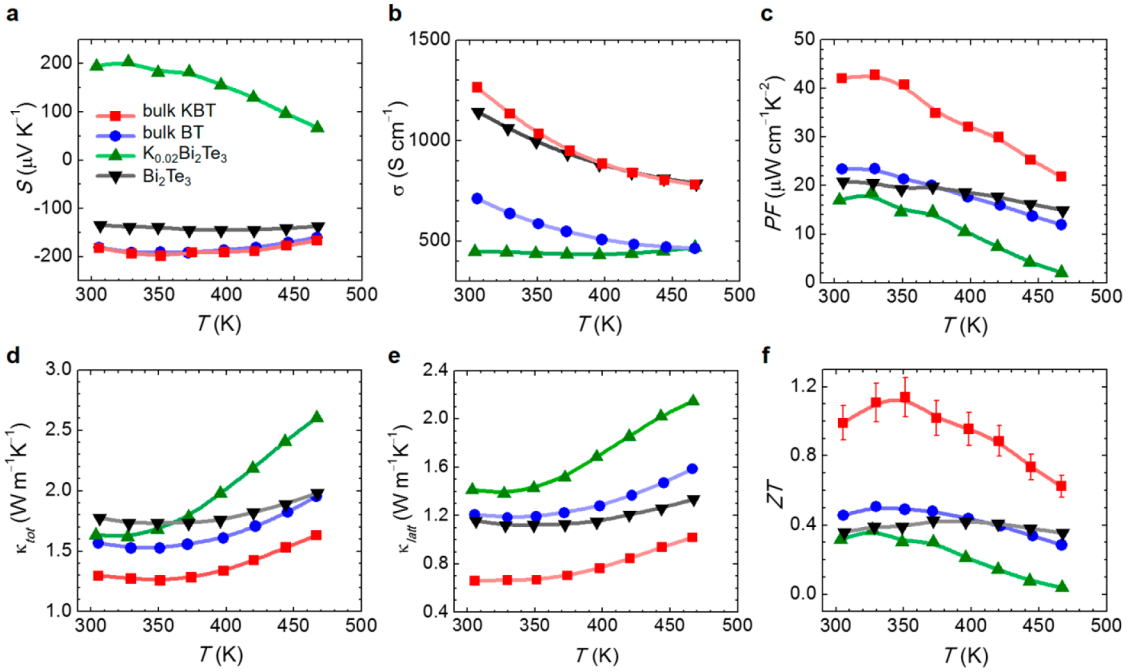

Figure 8. Thermoelectric properties taken perpendicular to the pressing direction of SPS (*ab* plane of Bi_2Te_3 structure) as a fuction of temperature for bulk BT and KBT in comparison with those of the control Bi_2Te_3 and $K_{0.02}Bi_2Te_3$ samples. All samples are SPS processed. (a) Seebeck coefficient (S), (b) electrical conductivity (σ), (c) power factor (PF), (d) total thermal conductivity (κ_{tot}), (e) lattice thermal conductivity (κ_{latt}), and (f) ZT values.

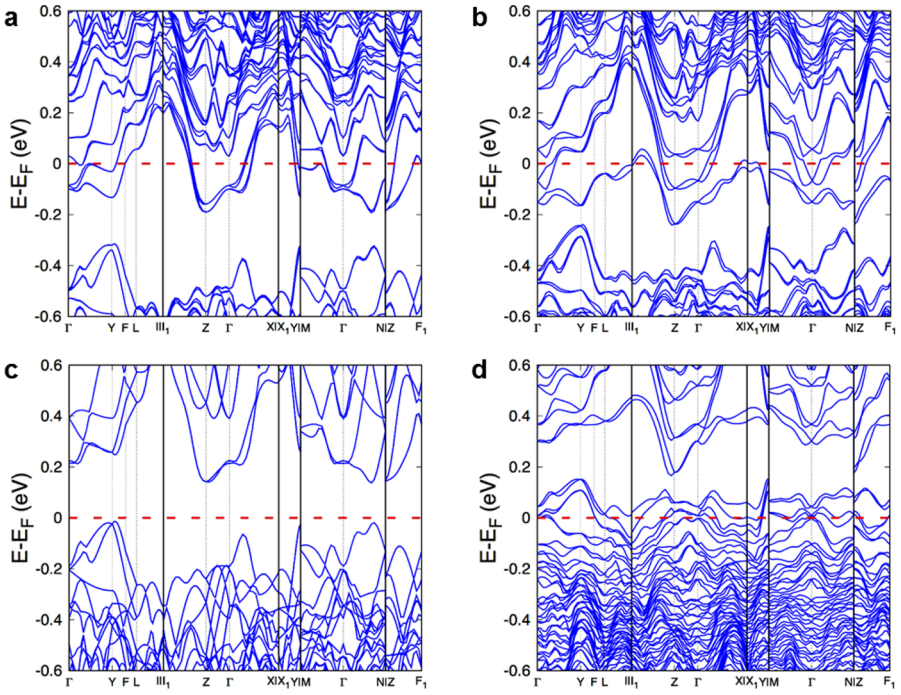

Figure 9. Calculated electronic structure of (a) $Bi_{35}Te_{55}$, a supercell of $Bi_2Te_{3.14}$ with Te_{Bi} defect, (b) $KBi_{35}Te_{55}$, a supercell of $K_{0.057}Bi_2Te_{3.14}$ with K_{int1} (potassium between Bi_2Te_3 layers) and Te_{Bi} defects, (c) $Bi_{36}Te_{54}$, a supercell of Bi_2Te_3, and (d) $KBi_{34}Te_{54}$, a supercell of $K_{0.058}Bi_2Te_{3.18}$ with K_{Bi} (potassium substituting Bi) and V_{Bi} (Bi vacancy) defects. The Fermi level is represented by the red dashed line.

Potassium atoms are not only much lighter than bismuth and tellurium atoms, but also their EELS spectrum significantly overlaps with that of carbon, making it difficult to directly differentiate the former from the latter. Carbon contamination is inevitable for cross-sectional sample preparation for STEM using focused ion beams. However, a previous study reports the clear differentiation of the carbon K edge and the potassium L_{23} edge of the EELS spectrum.[58] To confirm the presence and location of potassium atoms in bulk KBT layers, we carried out a STEM-EELS elemental scan profile at the atomic level. They occupy the interlayer space as well as the interstitial sites in Bi_2Te_3 layers according to the HAADF-STEM image coupled with the EELS spectrum (Figure 7f and S12). Since the contrast of HAADF-STEM images is roughly proportional to the square

DOI: 10.1021/jacs.6b09222
J. Am. Chem. Soc. 2016, 138, 14458−14468

of the atomic number (Z),[59] the atoms marked by arrows can be assigned as potassium. The interlayer gap increases from 0.27 to 0.32 nm, which provides enough space to adopt potassium at the octahedral sites (Figure S13). Moreover, the EELS spectrum affirms that the intercalated atoms pointed out by orange arrows are potassium.

Afterward, we conducted TE property characterization of the bulk BT and KBT samples. We also prepared control samples with nominal compositions of Bi_2Te_3 and $K_{0.02}Bi_2Te_3$ by the conventional high-temperature solid-state reaction. All of them were SPS processed and measured perpendicular to the press direction (highly oriented along the *ab*-plane direction of the Bi_2Te_3 structure). The temperature-dependent Seebeck coefficient (S) of the bulk BT, bulk KBT, and Bi_2Te_3 in the range 300−470 K is negative, indicating that electrons are the major charge carrier, i.e. n-type materials (Figure 8a). Because bulk BT and KBT cannot be obtained by conventional synthetic methods, it is important to understand the origin of their n-type conduction behavior. Accordingly, we calculated their electronic structures based on DFT by using the same defect conditions confirmed by the EELS and EDS results. The n-type characteristics of the bulk BT arise from the antisite defects of Te_{Bi} (Te atoms occupying a Bi lattice site) caused by the tellurium-rich composition ($Bi_2Te_{3.14}$), which is confirmed both experimentally by HAADF-STEM studies and theoretically by the following DFT calculations. We considered four types of point defects: Bi, Te vacancies are denoted as V_{Bi}, V_{Te}, respectively, and Bi, Te antisites are denoted as Bi_{Te}, Te_{Bi}, respectively. Our calculation verifies that Te_{Bi} is the most stable defect with the low formation energy of 0.379 eV under tellurium-rich condition. Such a defect condition is simulated in a supercell of $Bi_2Te_{3.14}$ (Figure S8). It causes a shift in the Fermi level into the conduction band, and results in an n-type electronic structure by DFT (Figure 9).

The unusual n-type behavior of bulk KBT is of paramount importance. In general, a high-temperature solid-state reaction distributes participating atoms statistically to form a thermodynamically stable phase. As a result, monovalent dopants that substitute higher-valent cations should induce p-type conduction as in the case of PbTe[60] and SnSe.[61] When potassium was introduced to Bi_2Te_3 via a solid-state reaction to form the control $K_{0.02}Bi_2Te_3$ sample, the expected p-type conduction was clearly observed due to the formation of substitutional acceptor defects (K_{Bi}). In contrast, potassium cations in the bulk KBT occupy the interlayer (K_{int1}) and interstitial sites (K_{int2}) according to the STEM-EELS results (Figure 7f and S12). DFT calculations reveal that K_{int1} pushes the Fermi level up to the conduction band to give an n-type electronic structure, whereas K_{Bi} shifts it down to the valence band to give a p-type electronic structure (Figure 9). To confirm this experimentally, we measured the electron concentration (n_e) and mobility (μ_e) by the Hall effect analysis. By incorporating potassium, the n_e value rises from $\sim 3.14 \times 10^{19}$ cm^{-3} (bulk BT) to $\sim 4.63 \times 10^{19}$ cm^{-3} (bulk KBT), and the corresponding μ_e value increases from ∼142 cm^2 V^{-1} s^{-1} to ∼171 cm^2 V^{-1} s^{-1} at 300 K (Figure S14), verifying that potassium acts as an excellent electron donor. In comparison, the control Bi_2Te_3 sample shows the n_e value of $\sim 4.79 \times 10^{19}$ cm^{-3} and the μ_e value of ∼164 cm^2 V^{-1} s^{-1} at 300 K.

Importantly, despite ∼1.5 times larger n_e of bulk KBT than that of bulk BT, both bulk BT and KBT samples have a comparable S value (−182 μV K^{-1}) at 300 K. This is in strong contrast with a typical transport behavior of TE materials in that the S value is inversely proportional to carrier concentration for heavily doped semiconductors.[51] Their S values at 300 K are significantly higher than that of the control Bi_2Te_3 sample (−135 μV K^{-1}). The unusual carrier type of potassium reflects the uniqueness of our nanochemical synthetic approach to develop bulk materials with unusual properties, which cannot be achievable by conventional preparative methods.

The effect of the potassium addition is evident in the σ value, nearly twice increased from ∼711 S cm^{-1} of bulk BT to ∼1265 S cm^{-1} of bulk KBT at 300 K (Figure 8b). This enhancement in σ can be attributed to the enhancement in both n_e and μ_e according to the Hall measurement. In contrast, when potassium is doped into Bi_2Te_3 to form the control $K_{0.02}Bi_2Te_3$ sample using a conventional solid-state reaction, the σ value significantly decreases from ∼1142 S cm^{-1} to ∼448 S cm^{-1}, demonstrating that very few dopants and substituents have proven effective in enhancing the thermoelectric performance of Bi_2Te_3-based materials.

The PF value of bulk KBT reaches a maximum ∼42.8 μW cm^{-1} K^{-2} at 323 K and decreases with further increasing temperature (Figure 8c). The PF value of bulk KBT is substantially larger than that of bulk BT (∼23.4 μW cm^{-1} K^{-2}), which is attributed to its higher σ with the comparable S value. It should be noted that the maximum value of bulk KBT is surprisingly close to ∼47 μW cm^{-1} K^{-2} of the single crystal sample and larger than ∼35 μW cm^{-1} K^{-2} of the state-of-the-art n-type $Bi_2Te_{3-x}Se_x$ materials.[52,62] In contrast, the control $K_{0.02}Bi_2Te_3$ sample exhibits a much lower PF value of ∼18.5 μW cm^{-1} K^{-2} at 323 K.

The total thermal conductivity (κ_{tot}) in Figure 8d shows that κ_{tot} of bulk KBT is lower than those of the other samples. Its minimum κ_{tot} value is ∼1.26 W m^{-1} K^{-1} at 350 K in comparison to ∼1.53 W m^{-1} K^{-1} of bulk BT. The κ_{tot} value of bulk KBT at 350 K measured parallel to the pressing direction of SPS (along the *c*-axis direction) is much lower at ∼0.51 W m^{-1} K^{-1} (Figure S15). Its ratio of $\kappa_{tot,ab\text{-}plane}/\kappa_{tot,c\text{-}axis}$ is ∼2.4, which is comparable to ∼2 of a $Bi_2Te_{3-x}Se_x$ (x = 0.075, 0.15) single crystal.[62] This is much greater than ∼1.5 for the highly oriented $Bi_2Te_{2.7}Se_{0.3}$ sample[62] that is ball-milled and then hot-pressed (BM-HP) multiple times to induce a high orientation. This significantly anisotropic thermal conduction agrees well with the highly oriented bulk KBT, as confirmed by powder X-ray diffraction patterns (Figure 4). We observe that the κ_{latt} value of bulk KBT (∼0.66 W m^{-1} K^{-1}) is much lower than that of bulk BT (∼1.21 W m^{-1} K^{-1}) at 300 K (Figure 8e). This can be explained by the cross-sectional HAADF-STEM and SEM images, revealing that various structural dislocations, such as strips of modulating Bi_mTe_n layers, broken atomic layers, and defect sites, are generated upon the incorporation of potassium (Figures 7c and S16). These dislocations act as effective scattering centers of heat-carrying phonons at the atomic- and nanoscale.

A TE figure of merit (ZT) value of bulk KBT at 300 K is ∼1.0, and increases to a maximum ZT of ∼1.14 at 350 K (Figure 8f), which is higher than the ZT values of the state-of-the-art n-type TE materials that operate near room temperature (Figure S17).[52,62] In fact, the ubiquitous tellurium defects in pure n-type Bi_2Te_3 are known to decrease PF, resulting in the reduction of ZT. High-ZT n-type Bi_2Te_3-based materials mostly contain Se or S,[63] which partially replaces Te to achieve enhanced PF and ZT values. However, alloying with smaller congeners of Te shifts the temperature of ZT_{max} higher due to

DOI: 10.1021/jacs.6b09222
J. Am. Chem. Soc. 2016, 138, 14458−14468

an increase in the band gap energy, resulting in a mismatch with that of the state-of-the-art p-type materials. For example, the best p-type $Bi_{0.5}Sb_{1.5}Te_3$ exhibits ZT_{max} at 340 K.[41] It should be noted that the high-TE performance of bulk KBT arises mainly from the enhanced *PF* derived from the electron donating potassium dopants, which is in strong contrast with the conventional synthetic methods for producing high-*ZT* TE materials.

■ CONCLUSION

In summary, we demonstrate that a new class of solid-state bulk compounds that do not obey the compositions dictated by phase equilibrium can be synthesized via nanochemistry. Potassium cations, which serve as unconventional electron donors, are key to the surprisingly high *PF* and the resulting high n-type TE performance. Using our current synthetic method, phase diagrams of solids can be largely reconstructed with a greatly expanded family of materials with novel physical and chemical characteristics for various applications.

■ EXPERIMENTAL SECTION

Starting Materials. The following reagents were used as obtained unless noted otherwise: tellurium dioxide (97.0%, Aldrich, US), bismuth(III) nitrate pentahydrate (98.0%, Aldrich, US), ethylene glycol (anhydrous, 99.8%, Aldrich, US), polyvinylpyrrolidone (PVP, average mol. wt. 40000, Aldrich, US), potassium hydroxide (90%, Aldrich, US), hydrazine hydrate solution (78−82%, Aldrich, US), acetone (99.9%, Aldrich, US), ethanol (99.8%, Aldrich, US), bismuth chunk (99.999%, 5N Plus, US), tellurium shot (99.999%, 5N Plus, US) and potassium chunk (99.5%, Aldrich, US).

Synthesis of Bi_2Te_3 Nanotubes. All syntheses were carried out under an Ar atmosphere using standard Schlenk line techniques. Bi_2Te_3 nanotubes were synthesized through a two-step solution reaction using a previously reported method after some modifications.[54] To synthesize tellurium-rich Bi_2Te_3 (BT) nanotubes, the precursor solutions of Bi and Te were separately prepared. The Te precursor solution was prepared by reacting 2.394 g of tellurium dioxide, 3 g of PVP, and 5.61 g of potassium hydroxide in 150 mL of ethylene glycol. The Bi precursor solution was prepared by dissolving 4.85 g of bismuth nitrate pentahydrate in 50 mL of ethylene glycol.

Te nanorods were synthesized by injecting 3 mL of hydrazine hydrate solution to the Te solution at 140 °C, followed by aging for 1 h. The solution was subsequently heated to 160 °C, and the Bi solution was added in a controlled manner. The resulting reaction mixture was aged for 30−60 min and cooled to room temperature. Fine control of the addition of the Bi solution and the reaction time is key to obtaining tellurium-rich Bi_2Te_3 nanotubes. The product was collected by centrifugation at 13000 rpm, followed by washing with ethanol and distilled water several times. To incorporate potassium, the as-synthesized BT nanotubes were reacted with 0.2 M potassium hydroxide−ethylene glycol solution under vigorous stirring at 140 °C for 24 h. Finally, the product was washed with acetone and dried under vacuum.

Synthesis of Control Bulk Powder. The control samples of Bi_2Te_3, Bi_2Te_{3+y}, and $K_xBi_2Te_{3+y}$ were obtained in bulk ingot form by melting a mixture of K/Bi/Te in an evacuated fused silica tube at 973 K for 12 h, followed by natural cooling to room temperature. The ingot samples were manually ground with a mortar and pestle in an Ar-filled glovebox.

Spark Plasma Sintering. The as-synthesized BT and KBT nanotubes and ground bulk powders were loaded into a graphite die in an Ar-filled glovebox and cold-compacted manually. The graphite die was taken out of the glovebox and placed in a spark plasma sintering system (SPS-211Lx, Fuji Electronic Industrial Co., Japan). The sample chamber was evacuated to a vacuum of ∼1.4×10^{-2} Torr, and powder samples in the graphite die were consolidated at ∼723 K for 5 min by spark plasma sintering under an axial pressure of 50 MPa in vacuum.

Powder X-ray Diffraction (XRD) and Infrared Spectroscopy. Powder XRD analysis was performed using a D/Max-2500 Rigaku powder X-ray diffractometer (Cu Kα radiation) operating at 40 kV and 100 mA.

To understand the structurally anisotropic nature of bulk KBT, we estimated its degree of preferential orientation perpendicular and parallel to the pressing direction of SPS, using the XRD patterns of bulk KBT (Figure 4). The Lotgering factor (LF) is commonly employed to quantify the degree of preferential orientation (texture) of a given material.[64] The LF is defined by eq 1:

$$LF = \frac{(p - p_0)}{(1 - p_0)}, \quad p = \frac{\sum I_{00l}}{\sum I_{hkl}} \tag{1}$$

where p is the degree of orientation for a preferential orientation, p_0 is the degree of orientation for a random orientation, and ΣI_{00l} and ΣI_{hkl} are the sums of peak intensities of the (00*l*) and (*hkl*) reflections in the 2θ range of 10° to 60°. For example, *LF* is 1 for a perfect (00*l*)-plane preferential orientation according to eq 1. For bulk KBT, the *LF* values of reflections taken perpendicular and parallel to the *ab*-plane are determined to be 0.78 and 0.11, respectively, indicating a highly anisotropic feature of bulk KBT.

Fourier transform infrared spectroscopy (FT-IR) spectra were recorded using a Vertex 70 Bruker FT-IR spectrometer equipped with a DLATGS detector and a KBr substrate with a multilayer coating beam splitter.

Thermal Analysis. Thermogravimetric analysis experiments were carried out on a Netzsch TG 209 F1 thermogravimetric analyzer by heating the samples in an alumina boat to 823 K at a rate of 10 K min^{-1} under Ar flow. The differential scanning calorimeter (DSC) measurements were performed on a Netzsch STA 449 F3 Jupiter DSC in an aluminum crucible with a lid under Ar flow to 973 K at a heating rate of 10 K min^{-1}.

Electrical Transport Properties. The samples after SPS were cut for electrical and thermal property measurements using a diamond saw and polished with ethanol using a polishing machine under N_2 atmosphere. The polished samples are rectangular-shaped with dimensions of ∼3 mm × 3 mm × 9 mm. The longer direction coincides with the direction in which the electrical conductivity is measured. The electrical conductivity σ and the Seebeck coefficient *S* were measured simultaneously under a He atmosphere from room temperature to ∼470 K on a ULVAC-RIKO ZEM-3 instrument system.

Thermal Conductivity. Thermal diffusivity (D) was directly measured under an Ar atmosphere, and the specific heat (C_P) was indirectly derived using a standard sample (Pyroceram) as a function of temperature from room temperature to ∼470 K using a flash diffusivity method in a Netzsch LFA 457 MicroFlash instrument. In a flash diffusivity method, the front face of a disk-shaped sample is irradiated by a short laser burst, and the resulting rear face temperature rise is recorded and analyzed by an IR detector. The thermal conductivity (κ) was calculated from the equation $\kappa = DC_P\rho$, where ρ is the density of the sample.

The total thermal conductivity κ_{tot} is the sum of the lattice (κ_{latt}) and electronic thermal (κ_{elec}) conductivities. κ_{elec} is proportional to the electrical conductivity (σ) according to the Wiedemann−Franz law ($\kappa_{elec} = L\sigma T$), where L is the temperature-dependent Lorenz number and T is the absolute temperature. An L value is estimated in the single parabolic band (SPB) model[65] from the temperature-dependent Seebeck coefficient, which is based on the assumption of acoustic phonon scattering. κ_{latt} is calculated from the relations described above.

Hall Measurement. The electron concentration (n_e) and the Hall coefficient (R_H) were measured by a Hall effect measurement system in the temperature range ∼173 K to ∼373 K using a Quantum Design physical property measurement system (PPMS-ECII). The samples were connected with four Pt wires using silver paste and loaded into a magnetic cryostat. The electron mobility (μ_e) was calculated from the

DOI: 10.1021/jacs.6b09222
J. Am. Chem. Soc. 2016, 138, 14458−14468

carrier concentration and the resistivity based on the assumptions of a single band model.

Chemical Analysis. Chemical compositions were determined by inductively coupled plasma atomic emission spectroscopy (ICP-AES) using Shimadzu ICPS-7500. To optimize the accuracy of the ICP-AES analysis of Bi and Te, we prepared stoichiometric Bi_2Te_3 by a high-temperature solid-state reaction to serve as the reference sample. For the preparation of the reference, the weight of Bi and Te elements was measured at a 10^{-4} gram scale. Using the Bi_2Te_3 reference, calibration curves were drawn for Bi and Te. More than 20 independent specimens per each material were measured and corrected by the calibration curve. The obtained values were averaged to give the chemical compositions of the materials.

Transmission Electron Microscopy (TEM). Cross-sectional samples for scanning TEM (STEM) were prepared for bulk BT and KBT by focused ion beams (FIB, Helios 650, FEG, FEI) with a dual beam microscope using gallium ion milling. Before the ion milling process, carbon was sputtered to preserve the sample by surface coating. The samples were further polished with a low-voltage and low-angle argon ion beam milling apparatus (NANO MILL, Model 1040, FISCHIONE). The atomic structures and chemical composition were examined using a spherical aberration-corrected JEM ARM-200F microscope (Cold FEG Type, JEOL) equipped with a SDD type energy dispersive X-ray spectroscopy (EDS) detector (Solid Angle 0.9-sr, X-MaxN 100TLE, OXFORD) and electron energy loss spectroscopy (EELS) detector (965 GIF Quantum ER, GATAN) at 200 kV.

In the high-angle annular dark-field (HAADF) STEM images, the point-to-point resolution was about 80 pm after the Cs-correction, and the angular range of the annular detector used was 68−280 mrad. All images were acquired with a high-resolution CCD detector using a 2k × 2k pixel device (UltraScan 1000, GATAN).

For STEM-EDS analyses, chemical maps were acquired with a probe size of 0.13 nm and a probe current of 40 pA. For STEM-EELS measurements, the energy dispersion was set at 0.1 eV ch^{-1}. The full-width at half-maximum of the zero-loss peak in vacuum was 0.6 eV. The convergence and collection semiangles were 19 and 52 mrad, respectively.

Scanning Electron Microscopy (SEM). The field emission scanning electron microscopy (FESEM) images were obtained on a JSM-6701F microscope.

Density Functional Theory (DFT) Calculations. The total energies and the optimized crystal structures were calculated by DFT with the PBEsol exchange-correlation functional[66] using the projector augmented wave method[67] implemented in the Vienna ab initio simulation package.[68] To calculate the defect formation energy, we used supercells of Bi_2Te_3 accommodating 90 atoms. Spin−orbit coupling was included in our electronic structure calculations. A plane-wave energy cutoff of 400 eV was used with the 6 × 6 × 4 *k*-points in the first Brillouin zone. Structural optimizations were performed with the force criterion of 1 meV $Å^{-1}$. For an accurate description of formation energy, we applied correction schemes for finite cell effects.[69]

To understand the conduction behavior of bulk BT and KBT, we calculated their electronic structures based on DFT by employing the same defect conditions confirmed by the EELS-EDS results. For bulk BT, we used $Bi_{35}Te_{55}$, a supercell of $Bi_2Te_{3.14}$, with the defects of Te_{Bi} (Te at the Bi site). For bulk KBT, we used $KBi_{35}Te_{55}$ with the defects of K_{int1} (potassium at the interlayer space of the Bi_2Te_3 lattices) and Te_{Bi}. DFT calculations result in n-type electronic structures for both bulk BT and bulk KBT (Figures 9a and b). In comparison, we calculated the electronic structure of K-doped bismuth telluride that possesses different types of defects: K_{Bi} (potassium substituting Bi) and V_{Bi} (Bi vacancy) along with that of undoped Bi_2Te_3 (Figures 9c and d). With this defect condition, $KBi_{34}Te_{54}$, a supercell of $K_{0.06}Bi_2Te_{3.18}$, reveals a p-type electronic structure by DFT.

To determine the solubility limit of potassium, we additionally calculated the formation energy of the potassium impurity. For simplicity, we only considered the single point-defect configurations of K_{int1}, K_{int2} (potassium at the interstitial site), and K_{Bi}. Based on the formation energies, the concentrations of potassium impurities were calculated under a tellurium-rich condition and a growth temperature at 800 K. The calculation results show that K_{Bi} is the most stable defect with a maximum solubility of 0.02% in the cationic site ($K_{0.0004}Bi_{1.9996}Te_{3.0073}$) (Figure S9).

■ ASSOCIATED CONTENT

Supporting Information

The Supporting Information is available free of charge on the ACS Publications website at DOI: 10.1021/jacs.6b09222.

Data of XRD, FT-IR, Hall measurement, DFT calculation, and additional TEM and SEM images (PDF)

■ AUTHOR INFORMATION

Corresponding Authors

*inchung@snu.ac.kr

*thyeon@snu.ac.kr

Author Contributions

#K.P. and K.A. equally contributed to this work.

Notes

The authors declare no competing financial interest.

■ ACKNOWLEDGMENTS

This work was supported by Institute for Basic Science (IBS-R006-D1). STEM measurements were performed at National Center for Inter-University Research Facilities SNU.

■ REFERENCES

(1) Bell, L. E. *Science* **2008**, *321*, 1457−1461.

(2) Dresselhaus, M. S.; Chen, G.; Tang, M. Y.; Yang, R. G.; Lee, H.; Wang, D. Z.; Ren, Z. F.; Fleurial, J. P.; Gogna, P. *Adv. Mater.* **2007**, *19*, 1043−1053.

(3) Zeier, W. G.; Zevalkink, A.; Gibbs, Z. M.; Hautier, G.; Kanatzidis, M. G.; Snyder, G. J. *Angew. Chem., Int. Ed.* **2016**, *55*, 6826−6841.

(4) Vineis, C. J.; Shakouri, A.; Majumdar, A.; Kanatzidis, M. G. *Adv. Mater.* **2010**, *22*, 3970−3980.

(5) He, J.; Sootsman, J. R.; Girard, S. N.; Zheng, J. C.; Wen, J.; Zhu, Y.; Kanatzidis, M. G.; Dravid, V. P. *J. Am. Chem. Soc.* **2010**, *132*, 8669−8675.

(6) Johnsen, S.; He, J.; Androulakis, J.; Dravid, V. P.; Todorov, I.; Chung, D. Y.; Kanatzidis, M. G. *J. Am. Chem. Soc.* **2011**, *133*, 3460−3470.

(7) Androulakis, J.; Todorov, I.; He, J.; Chung, D. Y.; Draivd, V. P.; Kanatzidis, M. G. *J. Am. Chem. Soc.* **2011**, *133*, 10920−10927.

(8) Zhao, L. D.; Lo, S. H.; He, J.; Li, H.; Biswas, K.; Androulakis, J.; Wu, C. I.; Hogan, T. P.; Chung, D. Y.; Dravid, V. P.; Kanatzidis, M. G. *J. Am. Chem. Soc.* **2011**, *133*, 20476−20487.

(9) Zeier, W. G.; LaLonde, A.; Gibbs, Z. M.; Heinrich, C. P.; Panthofer, M.; Snyder, G. J.; Tremel, W. *J. Am. Chem. Soc.* **2012**, *134*, 7147−7154.

(10) Zhao, L. D.; He, J.; Wu, C. I.; Hogan, T. P.; Zhou, X.; Uher, C.; Dravid, V. P.; Kanatzidis, M. G. *J. Am. Chem. Soc.* **2012**, *134*, 7902−7912.

(11) Zhao, L. D.; He, J.; Hao, S.; Wu, C. I.; Hogan, T. P.; Wolverton, C.; Dravid, V. P.; Kanatzidis, M. G. *J. Am. Chem. Soc.* **2012**, *134*, 16327−16336.

(12) Zeier, W. G.; Pei, Y.; Pomrehn, G.; Day, T.; Heinz, N.; Heinrich, C. P.; Snyder, G. J.; Tremel, W. *J. Am. Chem. Soc.* **2013**, *135*, 726−732.

(13) He, J.; Zhao, L. D.; Zheng, J. C.; Doak, J. W.; Wu, H.; Wang, H. Q.; Lee, Y.; Wolverton, C.; Kanatzidis, M. G.; Dravid, V. P. *J. Am. Chem. Soc.* **2013**, *135*, 4624−4627.

(14) Korkosz, R. J.; Chasapis, T. C.; Lo, S. H.; Doak, J. W.; Kim, Y. J.; Wu, C. I.; Hatzikraniotis, E.; Hogan, T. P.; Seidman, D. N.; Wolverton, C.; Dravid, V. P.; Kanatzidis, M. G. *J. Am. Chem. Soc.* **2014**, *136*, 3225−3237.

DOI: 10.1021/jacs.6b09222
J. Am. Chem. Soc. 2016, 138, 14458−14468

(15) Zhao, L. D.; Zhang, X.; Wu, H.; Tan, G.; Pei, Y.; Xiao, Y.; Chang, C.; Wu, D.; Chi, H.; Zheng, L.; Gong, S.; Uher, C.; He, J.; Kanatzidis, M. G. *J. Am. Chem. Soc.* **2016**, *138*, 2366−2373.
(16) Son, J. S.; Choi, M. K.; Han, M. K.; Park, K.; Kim, J. Y.; Lim, S. J.; Oh, M.; Kuk, Y.; Park, C.; Kim, S. J.; Hyeon, T. *Nano Lett.* **2012**, *12*, 640−647.
(17) Hsu, K. F.; Loo, S.; Guo, F.; Chen, W.; Dyck, J. S.; Uher, C.; Hogan, T.; Polychroniadis, E. K.; Kanatzidis, M. G. *Science* **2004**, *303*, 818−821.
(18) Biswas, K.; He, J. Q.; Zhang, Q. C.; Wang, G. Y.; Uher, C.; Dravid, V. P.; Kanatzidis, M. G. *Nat. Chem.* **2011**, *3*, 160−166.
(19) Ma, J.; Delaire, O.; May, A. F.; Carlton, C. E.; McGuire, M. A.; VanBebber, L. H.; Abernathy, D. L.; Ehlers, G.; Hong, T.; Huq, A.; Tian, W.; Keppens, V. M.; Shao-Horn, Y.; Sales, B. C. *Nat. Nanotechnol.* **2013**, *8*, 445−451.
(20) Biswas, K.; He, J. Q.; Blum, I. D.; Wu, C. I.; Hogan, T. P.; Seidman, D. N.; Dravid, V. P.; Kanatzidis, M. G. *Nature* **2012**, *489*, 414−418.
(21) Lee, Y.; Lo, S. H.; Androulakis, J.; Wu, C. I.; Zhao, L. D.; Chung, D. Y.; Hogan, T. P.; Dravid, V. P.; Kanatzidis, M. G. *J. Am. Chem. Soc.* **2013**, *135*, 5152−5160.
(22) Zhao, L. D.; Hao, S.; Lo, S. H.; Wu, C. I.; Zhou, X.; Lee, Y.; Li, H.; Biswas, K.; Hogan, T. P.; Uher, C.; Wolverton, C.; Dravid, V. P.; Kanatzidis, M. G. *J. Am. Chem. Soc.* **2013**, *135*, 7364−7370.
(23) Skoug, E. J.; Morelli, D. T. *Phys. Rev. Lett.* **2011**, *107*, 235901.
(24) Liu, H. L.; Shi, X.; Xu, F. F.; Zhang, L. L.; Zhang, W. Q.; Chen, L. D.; Li, Q.; Uher, C.; Day, T.; Snyder, G. J. *Nat. Mater.* **2012**, *11*, 422−425.
(25) Zhao, L. D.; Lo, S. H.; Zhang, Y. S.; Sun, H.; Tan, G. J.; Uher, C.; Wolverton, C.; Dravid, V. P.; Kanatzidis, M. G. *Nature* **2014**, *508*, 373−377.
(26) Zhao, L. D.; Tan, G. J.; Hao, S. Q.; He, J. Q.; Pei, Y. L.; Chi, H.; Wang, H.; Gong, S. K.; Xu, H. B.; Dravid, V. P.; Uher, C.; Snyder, G. J.; Wolverton, C.; Kanatzidis, M. G. *Science* **2016**, *351*, 141−144.
(27) Delaire, O.; Ma, J.; Marty, K.; May, A. F.; McGuire, M. A.; Du, M. H.; Singh, D. J.; Podlesnyak, A.; Ehlers, G.; Lumsden, M. D.; Sales, B. C. *Nat. Mater.* **2011**, *10*, 614−619.
(28) Banik, A.; Vishal, B.; Perumal, S.; Datta, R.; Biswas, K. *Energy Environ. Sci.* **2016**, *9*, 2011−2019.
(29) Jana, M. K.; Pal, K.; Waghmare, U. V.; Biswas, K. *Angew. Chem.* **2016**, *128*, 7923−7927.
(30) Zeier, W. G.; Schmitt, J.; Hautier, G.; Aydemir, U.; Gibbs, Z. M.; Felser, C.; Snyder, G. J. *Nat. Rev. Mater.* **2016**, *1*, 16032.
(31) Sales, B. C.; Mandrus, D.; Williams, R. K. *Science* **1996**, *272*, 1325−1328.
(32) Paschen, S.; Carrillo-Cabrera, W.; Bentien, A.; Tran, V. H.; Baenitz, M.; Grin, Y.; Steglich, F. *Phys. Rev. B: Condens. Matter Mater. Phys.* **2001**, *64*, 214404.
(33) Christensen, M.; Abrahamsen, A. B.; Christensen, N. B.; Juranyi, F.; Andersen, N. H.; Lefmann, K.; Andreasson, J.; Bahl, C. R. H.; Iversen, B. B. *Nat. Mater.* **2008**, *7*, 811−815.
(34) Kim, H.; Kaviany, M.; Thomas, J. C.; Van der Ven, A.; Uher, C.; Huang, B. L. *Phys. Rev. Lett.* **2010**, *105*, 265901.
(35) Shi, X.; Yang, J.; Salvador, J. R.; Chi, M.; Cho, J. Y.; Wang, H.; Bai, S.; Yang, J.; Zhang, W.; Chen, L. *J. Am. Chem. Soc.* **2011**, *133*, 7837−7846.
(36) Rogl, G.; Grytsiv, A.; Rogl, P.; Peranio, N.; Bauer, E.; Zehetbauer, M.; Eibl, O. *Acta Mater.* **2014**, *63*, 30−43.
(37) Prokofiev, A.; Sidorenko, A.; Hradil, K.; Ikeda, M.; Svagera, R.; Waas, M.; Winkler, H.; Neumaier, K.; Paschen, S. *Nat. Mater.* **2013**, *12*, 1096−1101.
(38) Beekman, M.; Morelli, D. T.; Nolas, G. S. *Nat. Mater.* **2015**, *14*, 1182−1185.
(39) Son, J. S.; Zhang, H.; Jang, J.; Poudel, B.; Waring, A.; Nally, L.; Talapin, D. V. *Angew. Chem., Int. Ed.* **2014**, *53*, 7466−7470.
(40) Poudel, B.; Hao, Q.; Ma, Y.; Lan, Y. C.; Minnich, A.; Yu, B.; Yan, X. A.; Wang, D. Z.; Muto, A.; Vashaee, D.; Chen, X. Y.; Liu, J. M.; Dresselhaus, M. S.; Chen, G.; Ren, Z. F. *Science* **2008**, *320*, 634−638.
(41) Kim, S. I.; Lee, K. H.; Mun, H. A.; Kim, H. S.; Hwang, S. W.; Roh, J. W.; Yang, D. J.; Shin, W. H.; Li, X. S.; Lee, Y. H.; Snyder, G. J.; Kim, S. W. *Science* **2015**, *348*, 109−114.
(42) Heremans, J. P.; Jovovic, V.; Toberer, E. S.; Saramat, A.; Kurosaki, K.; Charoenphakdee, A.; Yamanaka, S.; Snyder, G. J. *Science* **2008**, *321*, 554−557.
(43) Pei, Y. Z.; Shi, X. Y.; LaLonde, A.; Wang, H.; Chen, L. D.; Snyder, G. J. *Nature* **2011**, *473*, 66−69.
(44) Tang, Y.; Gibbs, Z. M.; Agapito, L. A.; Li, G.; Kim, H.-S.; Nardelli, M. B.; Curtarolo, S.; Snyder, G. J. *Nat. Mater.* **2015**, *14*, 1223−1228.
(45) Ahn, K.; Han, M.-K.; He, J.; Androulakis, J.; Ballikaya, S.; Uher, C.; Dravid, V. P.; Kanatzidis, M. G. *J. Am. Chem. Soc.* **2010**, *132*, 5227−5235.
(46) Zhang, Q.; Cao, F.; Liu, W.; Lukas, K.; Yu, B.; Chen, S.; Opeil, C.; Broido, D.; Chen, G.; Ren, Z. *J. Am. Chem. Soc.* **2012**, *134*, 10031−10038.
(47) Tan, G.; Zhao, L. D.; Shi, F.; Doak, J. W.; Lo, S. H.; Sun, H.; Wolverton, C.; Dravid, V. P.; Uher, C.; Kanatzidis, M. G. *J. Am. Chem. Soc.* **2014**, *136*, 7006−7017.
(48) Tan, G.; Shi, F.; Hao, S.; Chi, H.; Bailey, T. B.; Zhao, L. D.; Uher, C.; Wolverton, C.; Dravid, V. P.; Kanatzidis, M. G. *J. Am. Chem. Soc.* **2015**, *137*, 11507−11516.
(49) Banik, A.; Shenoy, U. S.; Saha, S.; Waghmare, U. V.; Biswas, K. *J. Am. Chem. Soc.* **2016**, *138*, 13068−13075.
(50) Rowe, D. M., Ed. *Thermoelectrics handbook: Macro to Nano*; CRC/Taylor & Francis: Boca Raton, FL, 2006.
(51) Sootsman, J. R.; Chung, D. Y.; Kanatzidis, M. G. *Angew. Chem., Int. Ed.* **2009**, *48*, 8616−8639.
(52) Liu, W. S.; Zhang, Q. Y.; Lan, Y. C.; Chen, S.; Yan, X.; Zhang, Q.; Wang, H.; Wang, D. Z.; Chen, G.; Ren, Z. F. *Adv. Energy Mater.* **2011**, *1*, 577−587.
(53) Massalski, T. B.; Okamoto, H.; Subramanian, P. R.; Kacprzak, L. *Binary Alloy Phase Diagrams*; ASM International: Materials Park, OH, 1990.
(54) Zhang, G.; Yu, Q.; Yao, Z.; Li, X. *Chem. Commun.* **2009**, 2317−2319.
(55) Yin, Y. D.; Rioux, R. M.; Erdonmez, C. K.; Hughes, S.; Somorjai, G. A.; Alivisatos, A. P. *Science* **2004**, *304*, 711−714.
(56) Jiang, Y.; Wang, Y.; Sagendorf, J.; West, D.; Kou, X.; Wei, X.; He, L.; Wang, K. L.; Zhang, S.; Zhang, Z. *Nano Lett.* **2013**, *13*, 2851−2856.
(57) Chung, I.; Malliakas, C. D.; Jang, J. I.; Canlas, C. G.; Weliky, D. P.; Kanatzidis, M. G. *J. Am. Chem. Soc.* **2007**, *129*, 14996−15006.
(58) Guan, L. H.; Suenaga, K.; Shi, Z. J.; Gu, Z. N.; Iijima, S. *Phys. Rev. Lett.* **2005**, *94*, 045502.
(59) Pennycook, S. J.; Jesson, D. E. *Phys. Rev. Lett.* **1990**, *64*, 938−941.
(60) Pei, Y. Z.; LaLonde, A.; Iwanaga, S.; Snyder, G. J. *Energy Environ. Sci.* **2011**, *4*, 2085−2089.
(61) Wei, T. R.; Tan, G.; Zhang, X.; Wu, C. F.; Li, J. F.; Dravid, V. P.; Snyder, G. J.; Kanatzidis, M. G. *J. Am. Chem. Soc.* **2016**, *138*, 8875−8882.
(62) Yan, X. A.; Poudel, B.; Ma, Y.; Liu, W. S.; Joshi, G.; Wang, H.; Lan, Y. C.; Wang, D. Z.; Chen, G.; Ren, Z. F. *Nano Lett.* **2010**, *10*, 3373−3378.
(63) Mehta, R. J.; Zhang, Y. L.; Karthik, C.; Singh, B.; Siegel, R. W.; Borca-Tasciuc, T.; Ramanath, G. *Nat. Mater.* **2012**, *11*, 233−240.
(64) Lotgering, F. K. *J. Inorg. Nucl. Chem.* **1959**, *9*, 113−123.
(65) May, A. F.; Toberer, E. S.; Saramat, A.; Snyder, G. J. *Phys. Rev. B: Condens. Matter Mater. Phys.* **2009**, *80*, 125205.
(66) Perdew, J. P.; Ruzsinszky, A.; Csonka, G. I.; Vydrov, O. A.; Scuseria, G. E.; Constantin, L. A.; Zhou, X.; Burke, K. *Phys. Rev. Lett.* **2008**, *100*, 136406.
(67) Blochl, P. E. *Phys. Rev. B: Condens. Matter Mater. Phys.* **1994**, *50*, 17953−17979.
(68) Kresse, G.; Joubert, D. *Phys. Rev. B: Condens. Matter Mater. Phys.* **1999**, *59*, 1758−1775.

DOI: 10.1021/jacs.6b09222
J. Am. Chem. Soc. 2016, 138, 14458−14468

(69) Lany, S.; Zunger, A. *Phys. Rev. B: Condens. Matter Mater. Phys.* **2008**, *78*, 235104.

DOI: 10.1021/jacs.6b09222
J. Am. Chem. Soc. 2016, 138, 14458−14468